PHYSICAL REVIEW ACCELERATORS AND BEAMS **26,** 103402 (2023)

Design, fabrication, and beam commissioning of a 216.667 MHz continuous-wave photocathode very-high-frequency electron gun

Lianmin Zheng, Han Chen, Bin Gao, Zixuan Dong, Zizheng Li, Yanqing Jia, Qili Tian,
Qianxu Xia, Yijiang Zhu, Jingjing You, Yingchao Du,[*] Lixin Yan, Jiaru Shi, Qingzi Xing,
Renkai Li, Wenhui Huang, Huaibi Chen, and Chuanxiang Tang

*Department of Engineering Physics, Tsinghua University, Beijing 100084, People's Republic of China
and Key Laboratory of Particle and Radiation Imaging, Tsinghua University,
Ministry of Education, Beijing 100084, People's Republic of China*

(Received 23 July 2023; accepted 10 October 2023; published 24 October 2023)

Tsinghua University is currently developing a very-high-frequency electron gun that operates in continuous-wave (cw) mode at 216.667 MHz. This gun will serve as the beam source for the Shanghai high repetition rate XFEL and extreme light facility. The cavity profile has been optimized to minimize input power, peak surface electric field, and peak wall power density. The profile optimization also takes into account the suppression of multipacting effect. Additionally, thermal analysis has been performed to guide the design of water cooling channels in coordination with gun mechanical design. The fabrication of the gun has been completed, and the frequency and quality factor measured in cold test are in good agreement with simulation expectations. During high power conditioning, 75 kW cw radio frequency power was successfully fed into the gun, corresponding to a cathode gradient of 27 MV/m and a gun voltage of 780 keV. This operating gradient is currently the highest in the world for room-temperature VHF guns. Under this condition, the maximum dark current collected by the Faraday cup at the gun exit was 376 nA when the strength of the gun solenoid was scanned. To measure and optimize the beam quality, a test beamline was constructed. After preliminary optimization, the 95% projected transverse emittance was 0.161 mm mrad for 10 pC bunches with a bunch length of 0.49 mm rms, 0.429 mm mrad for 50 pC bunches with a bunch length of 1.15 mm rms, and 0.853 mm mrad for 100 pC bunches with a bunch length of 1.44 mm rms.

DOI: 10.1103/PhysRevAccelBeams.26.103402

I. INTRODUCTION

X-ray free electron lasers (XFELs) [1–4] have played a crucial role in various fields such as physics, chemistry, structural biology, and material science. For example, the use of x-rays generated by XFELs as a probe has enabled direct observation of the fracture and formation of chemical bonds [5], analysis of protein structure and function [6,7], and visualization of material's femtosecond lattice dynamics [8]. One of the main directions for the further development of XFELs is to increase the duty cycle. In particular, increasing the repetition rate of the electron beam to MHz-class would be a revolutionary leap for the performance of XFELs. The MHz-class repetition rates significantly reduce the time required to collect data to accomplish an experiment and enable experiments that require a large number of photon pulse interactions. Over the past decades, multiple MHz repetition rate XFEL projects have been proposed and are rapidly developing.

The construction of the European XFEL was completed, and the first user experiment began in 2017 [4]. The European XFEL is capable of producing and accelerating trains of up to 2700 electron bunches within one 600 μs long radio frequency (rf) pulse, resulting in a repetition rate of 4.5 MHz for each rf pulse. The repetition rate of the rf pulse is 10 Hz, thus 27,000 electron bunches can be produced per second. LCLS-II [9] in the U.S. is the first MHz repetition rate XFEL project that has been proposed to work in continuous-wave (cw) mode. LCLS-II can produce 1 million electron bunches per second. LCLS-II is presently being commissioned. Furthermore, Shanghai high repetition rate x-ray free electron laser and extreme light facility (SHINE) [10] in China, an MHz repetition rate XFEL project working in cw mode, also began construction in 2018.

An L-band electron gun from DESY [11,12] is employed in the European XFEL. Due to the rf heating issue, the gun cannot operate in cw mode. There are three types of electron guns that can support cw operation of superconducting (SC) cryomodules of high repetition rate XFELs: direct-current (dc)

---

[*] dych@mail.tsinghua.edu.cn

TABLE I. Requirements of the SHINE facility for the gun rf parameters and the beam quality.

Parameters	Value	Unit
Gun operation mode	cw	
Cathode gradient	≥25	MV/m
Beam energy at the gun exit	≥750	keV
Bunch charge	10–300	pC
Beam repetition rate	1	MHz
95% normalized emittance for 100 pC @1 mm rms bunch length	<0.4	mm mrad
Dark current	<400	nA

guns [13,14], normal-conducting (NC) very-high-frequency (VHF) guns [15–18] and SC rf guns [19–22]. dc guns naturally have the flexibility to support high repetition rate operation, which can produce dc electron beams or bunches with any repetition rate. The cathode gradient of a state-of-the-art dc gun is 10 MV/m [23,24]. The gun voltage typically ranges from 200 to 500 kV [24,25]. It is noteworthy that Cornell University demonstrated that the electron beams produced from their 400 kV dc gun [13], with a cathode gradient of less than 5 MV/m using a low thermal emittance cathode, can meet the XFEL beam quality requirements.

The cavity wall power dissipation of an SC rf gun is orders of magnitude less than that of an NC rf gun, thus SC rf gun cw operation is easier to achieve. The compatibility of the SC rf environment of a cavity and the high quantum efficiency semiconductor cathode has been successfully demonstrated with an rf choke system [19–21]. Moreover, a dc-SC solution [26] was proposed and constructed by Peking University, which combines a dc gun and an SC acceleration unit, aiming to preserve the advantages of both dc and SC rf technologies. The potential of SC rf guns and dc-SC rf guns employed in XFELs is still being carefully evaluated.

NC VHF guns can operate in cw mode because a lower cavity frequency significantly reduces the power density on cavity walls, thus conventional water cooling techniques can solve the heat dissipation problem in cw mode. After several years of effort, the APEX gun developed by Lawrence Berkeley National Laboratory has achieved stable operation in cw mode [27], and the gun has demonstrated the capability to deliver the beam quality required for driving high repetition rate x-ray FELs [28]. The resonant frequency of the gun is 185.714 MHz. It can produce up to 300 pC electron bunches with 1 MHz repetition rates and 750 keV beam energy. The cathode gradient is about 20 MV/m. The success of the APEX gun proves the maturity of the VHF gun as an electron source for XFELs, and the APEX gun has been chosen as the electron source for LCLS-II [29].

SHINE is a high repetition rate XFEL facility based on an 8 GeV cw SC rf linac. Inspired by the success of the APEX gun, the SHINE facility chose a room temperature VHF gun as the electron source. The requirements of the SHINE facility for the gun rf parameters and the beam quality are displayed in Table I. Tsinghua University (THU) started developing VHF guns at the end of 2018. The gun will be employed as the electron source for SHINE. To date, we have completed the first phase of the beam commissioning, demonstrating good performance. The gun has been installed in the SHINE tunnel. This paper summarizes the details of the gun's research and development, including physical design, mechanical design and fabrication, cold test, high power conditioning, and beam commissioning, etc.

II. RF AND MULTIPACTING OPTIMIZATION

The gun resonant frequency should be compatible with the frequency of SHINE SC rf linacs (1300 MHz), i.e., 1300/n MHz, where n is an integer. Consequently, there are three frequency candidates in the VHF wave band: 216.667, 185.714, and 162.5 MHz. We have chosen 216.667 MHz as our gun's frequency based on the following considerations: (a) the frequency of the APEX gun (185.714 MHz) is not easily compatible with the existing XFEL timing system, and (b) a higher frequency has the potential to achieve a higher cathode gradient under the breakdown limit based on Kilpatrick's criterion [30].

To design the gun, we established a 3D model in CST MICROWAVE STUDIO, and all dimensions have been parametrized, as shown in Fig. 1. The gun shape was optimized using a built-in CST optimizer, with the frequency fixed at 216.667 MHz. We aim to achieve a 30 MV/m cathode gradient in the THU VHF gun. To reach this goal, the acceleration gap (*G* in Fig. 1) was reduced from the APEX gun's 4 to 3 cm, thus *G* is fixed at 3 cm in the optimization. The dimensions, except for *G*, were optimized simultaneously with defined constraints. The optimization goals include the gun voltage, the input power, the peak surface power density, and the peak surface electric field.

It should be noted that gun shape optimization must be combined with the need to suppress the multipacting effect. Multipacting refers to the exponential growth of secondary electrons in a resonant cavity under certain rf gradients [31,32]. Severe multipacting can damage the cavity's inner

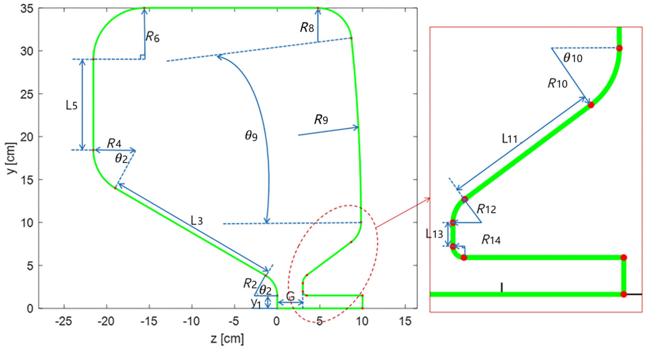

FIG. 1. Gun shape dimensions parameterized and optimized in CST.

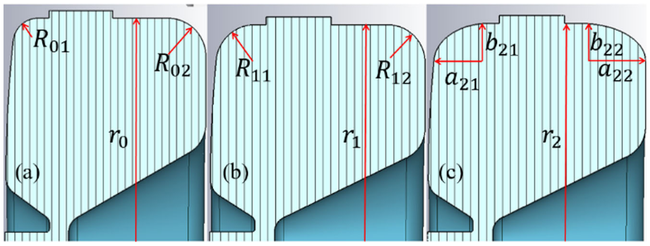

FIG. 2. Different gun shapes during multipacting optimization: (a) gun shape 1, (b) gun shape 2, (c) finalized gun shape.

surface and deteriorate the gun's operation. The multipacting effect in guns working in cw mode is more worthy of attention compared to guns working in pulse mode, because the continuous microwave feed-in in a cw gun can cause the secondary electrons to increase to a considerable amount, even at a low growth rate. Therefore, the multipacting effect in our gun must be carefully evaluated.

The multipacting was simulated in CST PARTICLE STUDIO with a tracking solver. Initially, some electrons are generated on the cavity's inner wall, and the rf field distribution is imported from CST MICROWAVE STUDIO. To suppress multipacting, we have designed various cavity shapes. We found that the multipacting zone is primarily located at the outer circle of the cavity shape (the region with a larger radius r) [16,17]. Therefore, we have optimized the dimensions of the gun shape related to the outer circle, including the cavity radius r, and the structure of the outer corners. Three typical cavity shapes are displayed in Fig. 2, and the corresponding key geometry parameters are listed in Table II. It is important to note that the other dimensions of each cavity shape have been optimized in CST MICROWAVE STUDIO, and the optimal rf parameters of all three gun shapes are acceptable. In addition, the magnetic field of the gun solenoid in the multipacting zone is extremely weak, even weaker than the geomagnetic field. Therefore, the solenoid magnetic field is not included in the multipacting simulation and only the gun rf fields are considered.

TABLE II. key geometry parameters of the three gun shapes in the multipacting optimization.

Gun shape 1	Gun shape 2	Finalized gun shape
$r_0 = 35$ cm	$r_1 = 33.5$ cm	$r_2 = 33.5$ cm
$R_{01} = 3.94$ cm	$R_{11} = 6$ cm	$a_{21} = 8.38$ cm
$R_{02} = 5.96$ cm	$R_{12} = 5.81$ cm	$b_{21} = 6$ cm
		$a_{22} = 10$ cm
		$b_{22} = 5.7$ cm

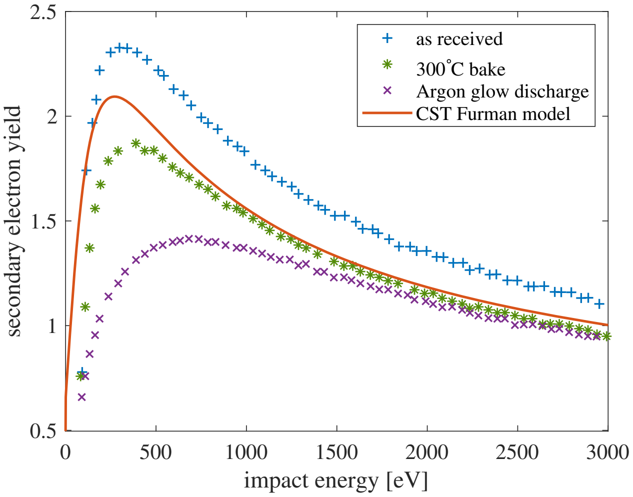

FIG. 3. Secondary emission yield of copper as a function of primary energy of electrons with different surface treatments [34]. The secondary electron yield based on the Furman model incorporated in CST is also plotted.

The secondary electron yield of copper varies with different surface treatments, and the secondary electron yield curves for copper with three different surface treatments are presented in Fig. 3. The secondary electron yield may further reduce in the rf conditioning process [33]. Additionally, the secondary electron yield based on the Furman model incorporated in CST is also included in Fig. 3. Since the secondary electron yield of copper cannot be accurately assessed during the design stage, and to be conservative, the CST Furman model was employed in the following simulations.

The evolutions of the total electron particles as a function of time can be calculated under different cathode gradients. If the number of particles increases exponentially with time, indicating that multipacting occurs in the gun, we can fit the growth curve with the equation $N_e(t) = N_0 \times e^{\alpha t}$, where $N_e(t)$ denotes the number of particles at time t, N_0 denotes the initial particle number, e denotes the natural base, and α denotes the growth rate, which can be used to characterize the multipacting intensity. If the number of particles decreases with time, indicating that no multipacting occurs, we set

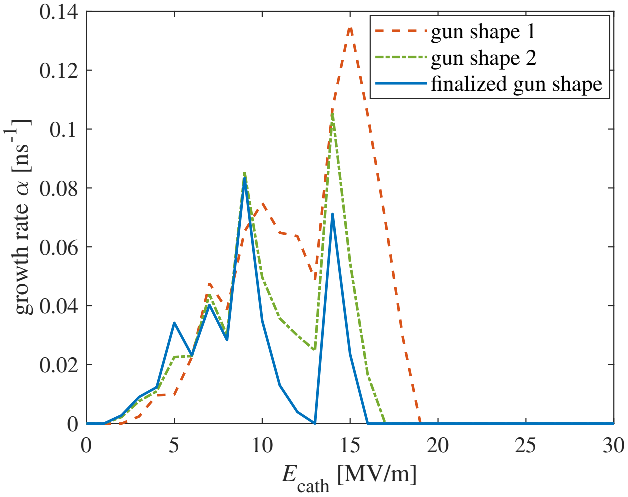

FIG. 4. Growth rate α of different gun shapes as a function of the cathode gradient E_{cath}.

TABLE III. Gun rf parameters after optimization.

Parameters	Value	Unit
Frequency	216.667	MHz
Cathode gradient	30	MV/m
Input power	90.4	kW
Peak surface electric field	37.0	MV/m
Peak surface power density	28.45	W/cm^2
Voltage	868	kV
Stored energy	2.24	J
Quality factor	33717	
Shunt impedance	8.34	MΩ

$\alpha = 0$ for convenience. The exponential growth rate α of the three gun shapes as a function of the cathode gradient is shown in Fig. 4.

First, we reduced the cavity radius from 35 to 33.5 mm and increased the anode outer corner radius [from Figs. 2(a) to 2(b)]. As shown in Fig. 4, the multipacting intensity was significantly reduced. Building on this success, we changed the outer circle from circular to elliptical, as shown in Fig. 2(c), and we found that the multipacting intensity was further reduced. This finalized gun shape [Fig. 2(c)] is the basis for our mechanical design. As shown in the blue line in Fig. 4, there is no multipacting when the cathode gradient is larger than 16 MV/m. The rf parameters of our gun are shown in Table III, and the corresponding electric and magnetic field distributions are depicted in Fig. 5.

In the above simulation, the corners at the joints of the cathode plug and the copper base plate were not considered. These corners can result in electric field enhancement compared to E_{cath} and become the main source of dark current downstream of the gun. As these corners are close to the gun axis center, the dark current emitted from these corners is more easily transported out [35]. Figure 6 illustrates the electric field distributions at the corners of the joints of the cathode plug and the copper base plate with two corner shapes. The first is a round corner with a radius of 1 mm, which is the same as the APEX gun [15]. The second is an elliptical corner with a major axis of 1.5 mm and a minor axis of 0.5 mm. If the electric field at the center of the cathode plug is 30 MV/m, the peak surface electric field at the round corner is 37 MV/m while the peak surface electric field at the elliptical corner is 32.5 MV/m. Therefore, the elliptical corner has been adopted for our gun, which helps to suppress dark current emission and reduce the possibility of breakdown in this region.

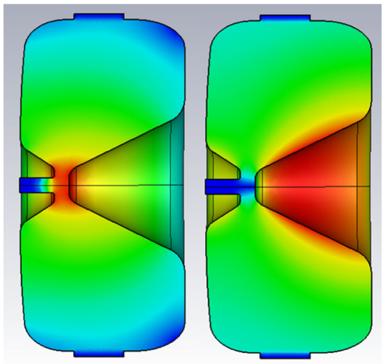

FIG. 5. Electric (left) and magnetic (right) field distributions in the gun.

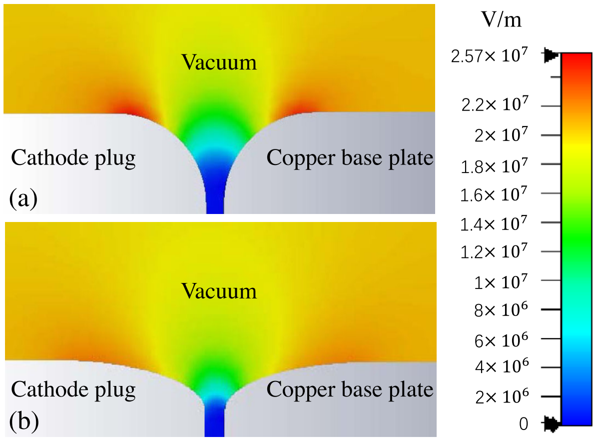

FIG. 6. Electric field distributions at the corners of the joints of the cathode plug and the copper base plate with (a) round corners and (b) elliptical corners.

III. MECHANICAL DESIGN AND MULTIPHYSICS ANALYSIS

The mechanical design of the gun is illustrated in Fig. 7. The structure is similar to the APEX gun but with some

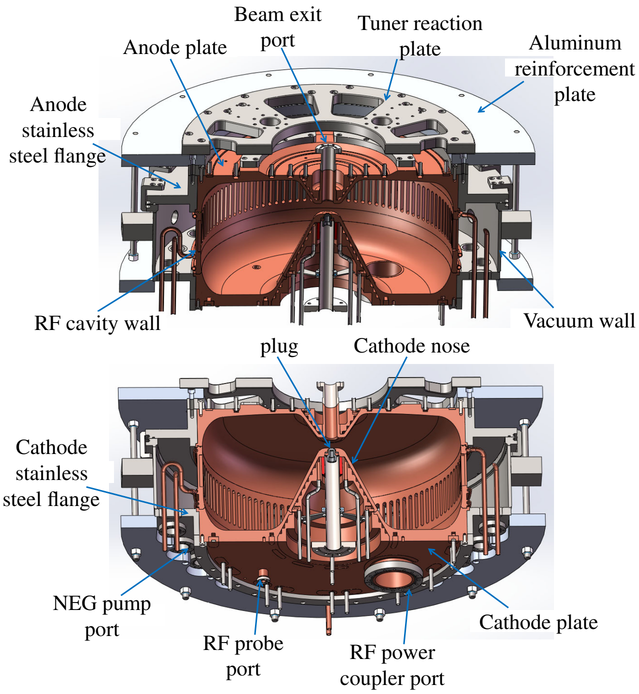

FIG. 7. VHF gun cross sections.

modifications based on our manufacturing experience. The cavity structures are machined with oxygen-free electrolytic copper, while the vacuum chamber, including the vacuum wall and the large flanges on the cathode and anode, and all Conflat (CF) flanges and vacuum pipes, are machined with 316L stainless steel. This material has low permeability, which reduces the negative impact of residual magnetic fields on the beam quality.

An array of 108 slots measuring 10 mm in width, 14 mm in depth, and 100 mm in length are milled through the rf cavity wall to connect the cavity and the stainless steel vacuum chamber. There are 24 CF 35 flanges electron beam (Ebeam) welded to the large cathode stainless steel flange for connection to the vacuum pumps, including 20 Capacitorr Z400 NEG pumps and 4 NexTorr NEG-ion pumps from SAES. Additionally, there are one CF 150 flange and six CF 35 flanges on the vacuum wall, where the CF 150 flange is used to connect a 300 L/s ion pump and the six CF 35 flanges are used to connect rough pumping valves, residual gas analyzer, vacuum gauges, etc. Based on this vacuum configuration, a MOLFLOW+ [36] simulation shows that the vacuum at the plug top surface can reach 1.45×10^{-8} Pa. There are two CF 100 flanges and two CF 16 flanges on the cathode plate, where the CF 100 flanges are used to connect rf power couplers and the CF 16 flanges are used to connect RF probes. Two aluminum reinforcement plates are installed on the cathode and anode stainless steel flanges, respectively, and then connected by twelve 16 mm threaded rods to enhance the gun's overall rigidity. Two semicircular tuner reaction plates machined from 7075 aluminum alloy are installed on the anode side to connect the frequency tuners.

The VHF gun has a high average power, which requires careful analysis of the rf thermal effects to ensure stable operation. Complex water cooling channels are designed to carry away the rf heat dissipated on the surface of the copper inner wall. The gun has 23 independent cooling channels, as shown in Fig. 8.

The cathode nose of the VHF gun features two parallel spiral cooling channels with 3.5 turns. The nose is composed of two cones, with the outer cone in contact with the microwave and the inner cone featuring spiral channels milled into its surface. The inner and outer cones are brazed using a hydrogen furnace. The spiral channel profile is designed as a triangle to optimize the compact space within the nose. Similarly, the cathode plate has two parallel spiral cooling channels with 1.5 turns in its center, milled into the surface of the inner cone with a triangular profile. The inner cone is Ebeam welded onto the cathode plate. Additionally, the cathode plate has ten water cooling channels formed by radially drilling holes. In areas not covered by radial drillings, slots are dug on the back of the cathode plate and copper covers are Ebeam welded to achieve complete cooling channels.

On the rf cavity wall, there are three copper tubes with an outer diameter of 12 mm and an inner diameter of 8 mm, TIG welded to the wall. The anode plate has a small nose in its center with a cooling channel formed by two parallel spiral channels with 2 turns converging at the top of the nose. The water passage is milled into the surface of the inner cone, which is Ebeam welded onto the anode plate. The anode plate also has five cooling channels located on four circles. Three cooling channels are located on the three inner circles. The water inlet and outlet are located on both sides of the circles, splitting the flow into two parallel paths. The outermost circle is divided into two semicircular channels with no connection between them. These five channels are formed by digging slots on the back of the anode plate and Ebeam welding copper covers.

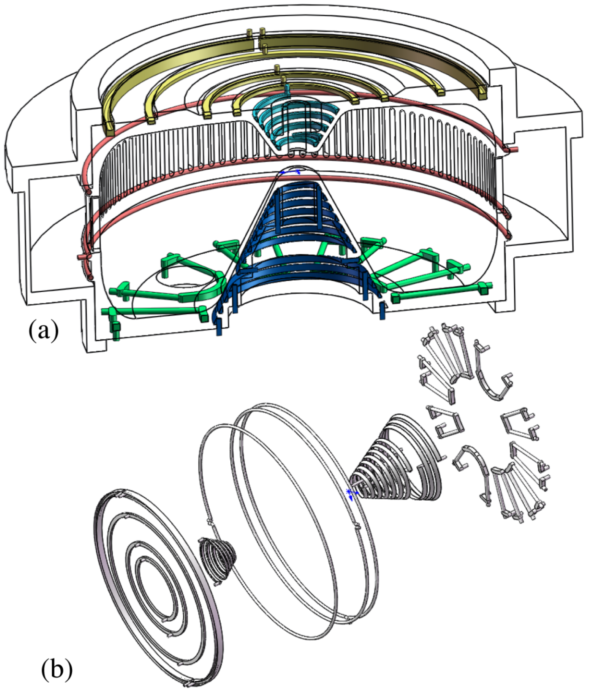

FIG. 8. (a) Water cooling channels in the gun marked by different colors. (b) Explosion view of 23 cooling channels.

The VHF gun undergoes coupled electromagnetic-thermal-structural finite element analysis using ANSYS [37]. The rf parameters are simulated in HFSS, with a total rf surface loss of 90.4 kW assumed on the cavity wall and the loss distribution imported into Fluent as a heat source. The water flow rate of the two spiral channels in the cathode nose is assumed to be 15 L/min, while the other 21 channels have a flow rate of 10 L/min. The flow velocity of the two spiral channels in the cathode nose is 5.9 m/s, and the flow velocity of the other 21 channels ranges from 2.1–3.3 m/s depending on the cross-sectional area of different water passages. The water initial temperature at inlet is assumed to be 28 °C, and a k-epsilon model is employed to consider turbulence in water flow. At water inlet the turbulent intensity is assumed to be 5%, and the turbulent viscosity ratio is assumed to be 10. The steady-state temperature distributions of the VHF gun are shown in Fig. 9.

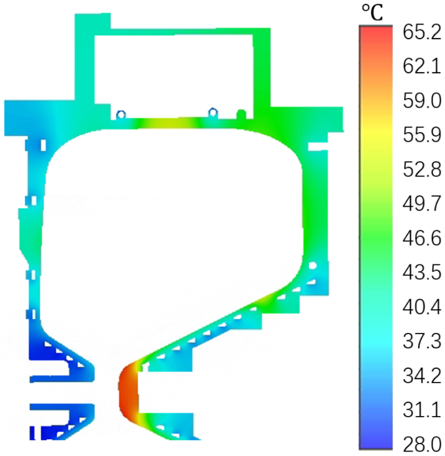

FIG. 9. The steady-state temperature distribution on a cross section of the VHF gun.

The highest temperature is 65.2 ℃, located at the top of the cathode nose. The temperature at the slots on the rf cavity wall is also high, about 54 ℃. The temperature in other locations is below 50 ℃. The temperature rise of all the cooling channels is below 9 ℃. The pressure drop between the outlet and the inlet of all the cooling channels is below 0.15 MPa.

The temperature distribution calculated in Fluent is then imported into the static structural module for mechanical simulations. The beam exit port at the center of the anode plate is assumed to be fixed as a reference point in the simulation. Since the fixed point is connected to the gun body through a thin copper pipe with low strength, the gun is essentially free to deform without any constraints. The deformation due to thermal expansion is depicted in Fig. 10, with the deformation decomposed into radial and axial components. The radial deformation is characterized by an approximately linear expansion. For example, the slots on the rf cavity wall expand by 135 μm and the surface of the cathode nose also expands by 30 μm. The radial expansion leads to a frequency decrease of about 95 kHz. In addition, the axial deformation of the anode plate is small. Due to the axial thermal expansion of the slots on the rf cavity wall, the cathode plate moves backward by about 160 μm. Simultaneously, the cathode nose undergoes thermal expansion and moves forward relative to the cathode plate. The change in the cathode-anode gap is small, with only a slight increase of 29 μm. These axial movements result in a frequency increase of about 34 kHz. In summary, the frequency decreases by about 61 kHz due to the thermal deformation.

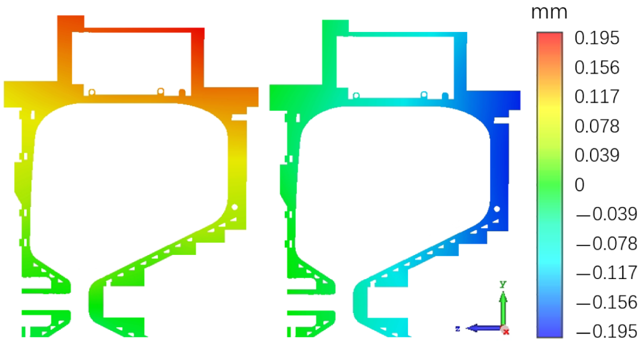

FIG. 10. Radial (left) and axial (right) deformation of the VHF gun due to thermal expansion.

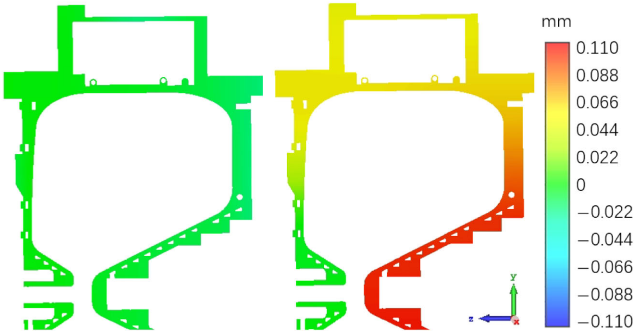

FIG. 11. Radial (left) and axial (right) deformation of the VHF gun due to atmospheric pressure.

The VHF gun’s radial and axial deformation due to atmospheric pressure is shown in Fig. 11. The radial deformation is very small. Under atmospheric pressure, both the cathode assembly and the anode assembly are inwardly concave, resulting in a 110 μm decrease in the cathode-anode gap and a frequency reduction of about 100 kHz.

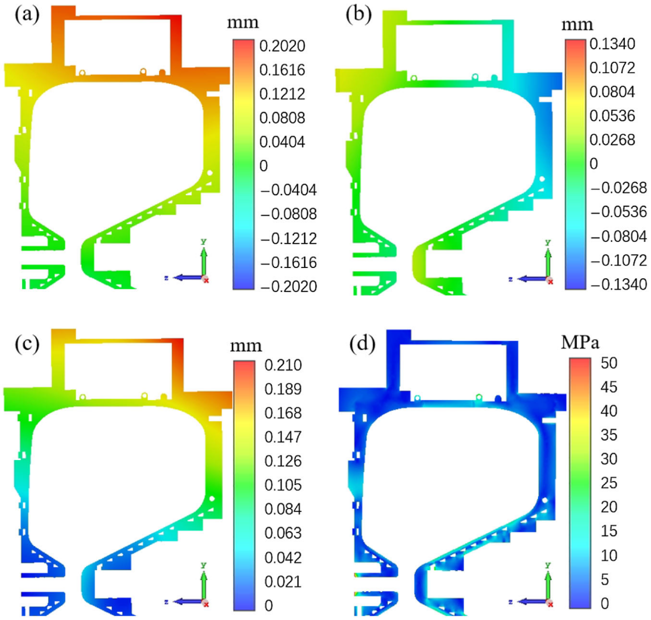

FIG. 12. Radial (a), axial (b) and total (c) deformation of the VHF gun due to thermal expansion and atmospheric pressure. The distribution of the von Mises equivalent stress is also shown in (d).

The radial, axial, and total deformations of the VHF gun due to both thermal expansion and atmospheric pressure are shown in Fig. 12. In addition, the distribution of the von Mises equivalent stress is also shown in Fig. 12(d). The maximum stress of the copper cavity body is 36 MPa, safely below the yield strength.

IV. GUN ASSEMBLY

During the final assembly process, the VHF gun is divided into two parts: the cathode assembly and the anode assembly. The cathode assembly is welded together in the following steps: (i) Ebeam welding the vacuum wall to the cathode stainless steel flange, (ii) Ebeam brazing the cathode plate to the cathode stainless steel flange, (iii) Ebeam welding the cathode nose to the cathode plate, and (iv) Ebeam welding the rf cavity wall to the cathode plate. The anode assembly consists of the anode plate and the anode stainless steel flange, which are Ebeam brazed together.

After welding, the inner surfaces of the copper cavity in both the cathode and anode assemblies still have 1.5 mm of extra material. The inner cavity surfaces are then milled to their final dimensions. The anode and cathode assemblies after final machining are shown in Fig. 13. The machining accuracy of the inner cavity surface is measured by a coordinate measuring machine, and the results are shown in Fig. 14. The machining error of the inner cavity surface is within 25 μm for the anode assembly and within 15 μm for the cathode assembly.

Similar to the APEX gun, a square groove was machined into the end face of the cavity wall to hold a gold-plated stainless steel canted-spring-ring. The inside of the groove is 0.25 mm higher than the outside. Once the cavity is assembled, the end face inside the groove bears against the end face of the anode plate, to form a primary rf contact. Moreover, the spring ring serves as a secondary rf contact for added reliability.

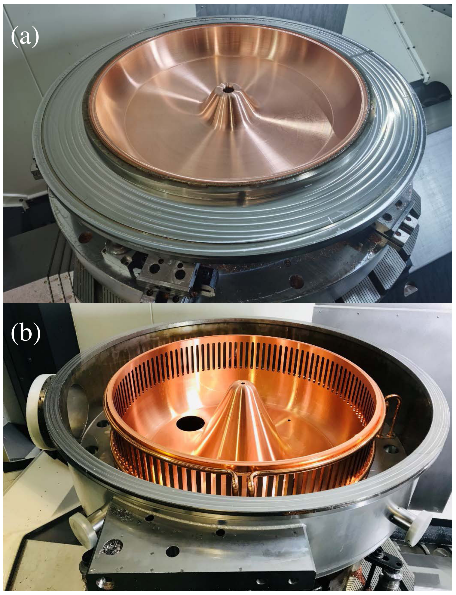

FIG. 13. The anode assembly (a) and cathode assembly (b) after final machining.

At this point, the end face at the rim of the anode plate still retains 300 μm of extra copper material. When the cathode and anode are assembled together, the gap between the cathode nose and the anode is larger than the design value, thus the frequency is higher than the target frequency. The extra material is then removed step by step to reduce the gap until the gun frequency reaches the target frequency. Vector network analyzer measurements show that the relationship between the thickness of the removed material and the reduction of frequency is 1 kHz/μm.

After final machining, the inner cavity surface is manually polished to reduce roughness. All inner cavity surfaces for both the anode and cathode assemblies are polished to a mirror finish with an rms roughness of 0.05 μm or less. The cathode and anode assemblies then go through a multistage cleaning procedure that includes ultrasonic cleaning, dry-ice cleaning, and ultrapure water rinsing. After the cathode and anode are assembled together, the cathode-anode coaxiality is adjusted using a laser tracker, and the final coaxiality is less than 50 μm. Finally, the stainless steel rims where the vacuum wall and the anode flange contact are TIG welded together to ensure vacuum sealing.

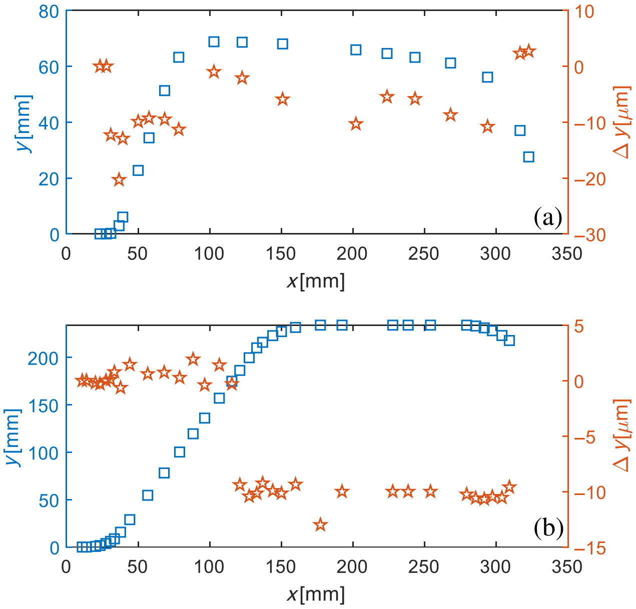

FIG. 14. Machining accuracy measurement results of the inner cavity surface for anode assembly (a) and cathode assembly (b) The squares indicate the measured inner cavity profile and the stars indicate the machining accuracy.

V. ANCILLARY COMPONENTS

A. rf power couplers and probes

RF power couplers play a crucial role in transferring rf energy from the solid-state power source to the VHF gun. The mechanical structure of the coupler is illustrated in Fig. 15. The coupler body is an L-shaped 4-1/16 inch coaxial waveguide. The waveguide's outer conductor is divided into three sections, all connected by CF100 flanges. The inner conductor, on the other hand, is divided into two sections, joined together by a dual-tenon adapter. Two magnetic loops connecting the inner and outer conductors are used for power coupling at the end of the waveguide near the VHF gun side. The upper inner conductor is connected to the coupling loops through a pipe, so there is a water cooling channel to cool both the loops and the upper inner conductor. Three ceramic pillars under the loops provide additional support for the upper inner conductor. A ceramic window is welded to isolate the vacuum and atmosphere. There is a water cooling channel to cool the outer conductor connected to the window. The lower inner conductor is supported by the window. A cuboid aluminum box on the atmosphere side is designed to allow the cooling of the lower inner conductor. Both the inner and outer conductors of the box have a cuboid shape. The box has three ports, one port is connected to the window, one port is connected to the SSA via a waveguide, and the last port is an rf terminated port. The cooling pipe of the lower inner conductor on the window passes through the interior of the inner conductor of the cuboid box, continues through the rf terminated port, and finally connects to an external water unit. The dimensions of the two cuboids and the length of the rf terminated port are systematically optimized to match the microwave transmission, and the power reflection at the waveguide port after optimization is less than 1%. The inner and outer conductors on the vacuum side are vapor coated with titanium nitride to suppress secondary electron emission. Two CF 35 flanges are mounted on the outer conductor for vacuum pumping. Typically we install NEG-ion pumps in this position. In addition, two CF 16 flanges are mounted on the outer conductor, one for mounting a breakdown monitor and the other for mounting a micro-current monitor. The breakdown monitor is connected to an interlock protection system to cut off the power source output in time when a breakdown occurs inside the coupler or VHF gun. The microcurrent monitor is a small electrical probe that can be connected to an oscilloscope to monitor multipacting intensity inside the coupler.

Two identical couplers are installed on the VHF gun, and the coupling factor of each coupler can be adjusted by rotating the coupling loop. We usually need to adjust the coupling factor of each coupler to 0.5, so that the total coupling factor β is 1. Figure 16 shows the total coupling factor β versus the rotation angle of the coupling loop in CST simulation. The total coupling factor can be up to 2.7. In practice, the coupling loop should be placed close to the horizontal (0° in Fig. 16) to enable a total coupling factor of 1.

Two electric probes are also equipped on the VHF gun, and the coupling factor can be flexibly adjusted by changing the probe length. Generally, one probe is connected to the digital low-level rf (LLRF) system for closed-loop control, while the other probe is connected to an oscilloscope for real-time monitoring of the gun power.

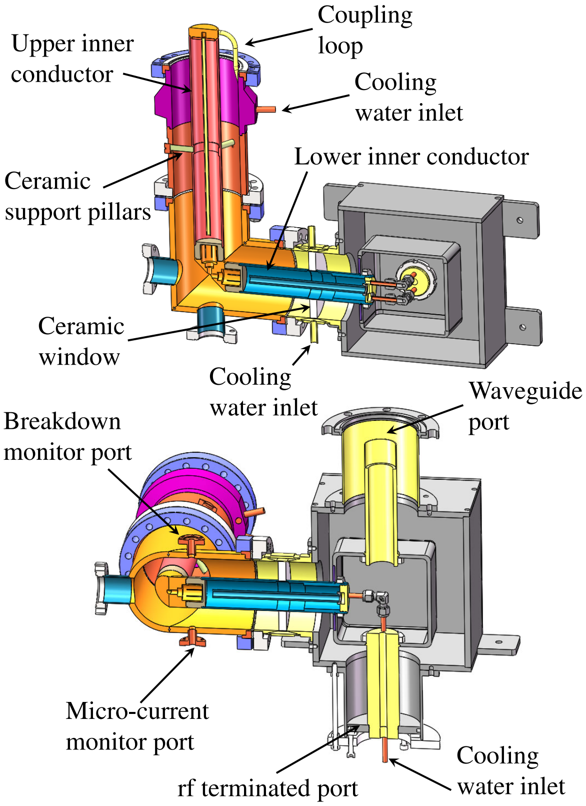

FIG. 15. Rf power coupler cross sections.

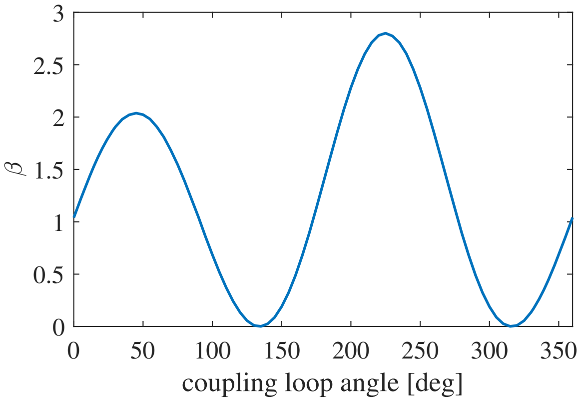

FIG. 16. The total coupling factor β versus rotation angle of the coupling loop in CST simulation. 0 degree indicates that the coupling loop is in the horizontal direction.

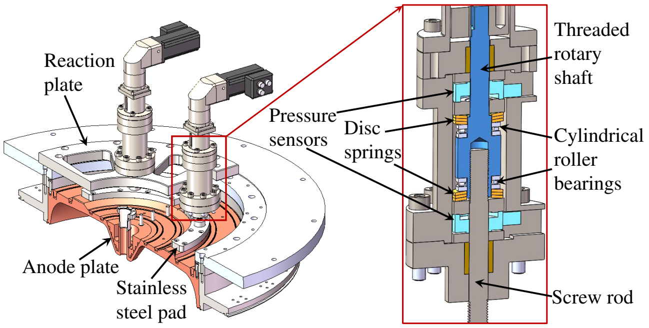

FIG. 17. Model of the tuners (2 of 4 shown) mounted on the anode assembly. One of the two reaction plates is not shown here, in order to demonstrate the connection of the tuner to the anode plate. A partial cross section illustrates the internal structure of the tuner.

B. Frequency tuners

During VHF gun operation, the resonant frequency is stabilized by adjusting the cathode-anode gap through the elastic deformation of the anode plate. The elastic deformation is achieved by pulling or pressing the anode plate through four tuners. A model of the tuners mounted on the anode assembly is shown in Fig. 17.

The base of the tuner is mounted on the reaction plate and bolted to the aluminum reinforcement plate and the large anode stainless steel flange. The anode plate is mounted with four stainless steel pads, with a screw rod at the center of the tuner connected to the stainless steel pad. The tuners apply force to the anode plate through these pads. A cross section of the tuner is also shown in Fig. 17 to illustrate the internal structure. During operation, a stepper motor drives a threaded rotary shaft to rotate. The rotary shaft is threadedly connected to the screw rod. The screw rod is fixed to the stainless steel pad and cannot rotate. Therefore, the screw rod can only move up and down and apply tension or pressure to the anode plate when the motor moves. There are some auxiliary components inside the tuner, including two cylindrical roller bearings, two sets of disc springs and two pressure sensors. The roller bearings can reduce the resistance of the rotary shaft when it rotates. Two sets of disc springs are mounted against the two bearings, and a force of less than 1 kN is applied to the internal components of the tuner by the deformation of the disc springs during the preassembly. Two pressure sensors inside the tuner are used to measure the force applied to the anode plate. In the initial state, the forces of the two sensors are equal, indicating that no force is applied to the anode plate. When the motor starts to move, the force of one pressure sensor becomes larger and the other becomes smaller. The difference between the two pressure sensors indicates the state of applied force to the anode plate. Each tuner is capable of delivering up to 13 kN push or pull force on the anode plate. However, we limit the force of each tuner to 11 kN during operation for safety reasons.

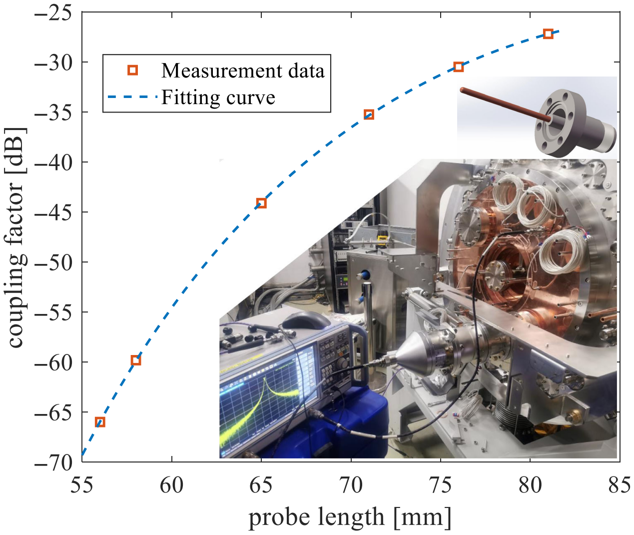

FIG. 18. The red squares indicate the measurement data of the coupling factor of the probe as a function of the probe length. The blue dashed line is a fitting of the measurement data. The inset shows the cold test photo and the model of the probe.

VI. COLD TEST

The coupling of the electric probes was measured using a vector network analyzer. The inset of Fig. 18 presents a cold test photo and a model of the probe. The center of the probe is a 3 mm diameter copper rod. The rod is threadedly connected to the probe base, so it can be easily removed and replaced. The head of the rod is machined into a rounded shape to reduce the possibility of breakdown. We

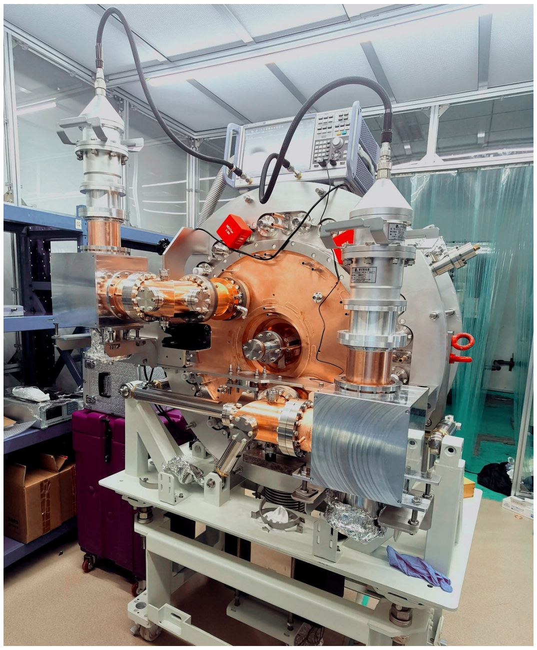

FIG. 19. Cold test photo for measuring and adjusting the coupling of the rf power couplers.

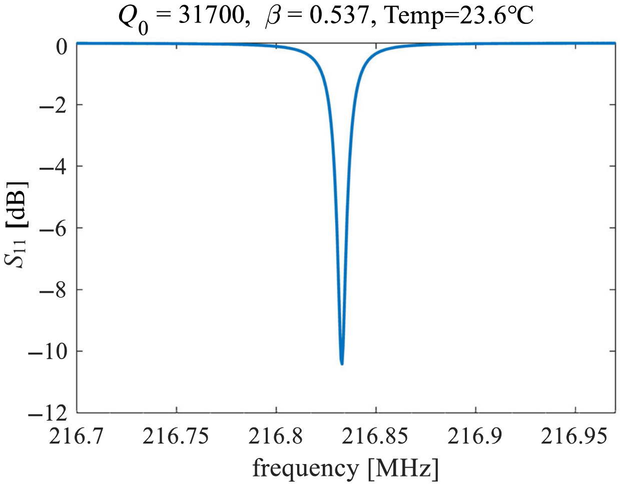

FIG. 20. S_{11} measurement of the VHF gun with one coupler port connected to the vector network analyzer and the other coupler port short-circuited.

replaced the copper rod with different lengths and measured the coupling factor, and the results are demonstrated in Fig. 18.

The coupling factor of both probes was tuned to be about −60 dB, in other words, each probe can couple out 90 mW of power when there is 90 kW of power in the gun. This power is sufficient for our LLRF system.

Next, the coupling of the rf power couplers was measured and adjusted. A cold test photo is depicted in Fig. 19. For ease of reference, the coupler located at the bottom right was named Coupler 1, while the coupler at the top left was named Coupler 2. First, the port of Coupler 1 was connected to the vector network analyzer and the port of Coupler 2 was short-circuited. The S_{11} curve was repeatedly measured while the coupling loop of Coupler 1 was rotating, and the coupling factor and quality factor were calculated from the S_{11} curve. The S_{11} curve after the coupling factor adjustment of Coupler 1 is shown in Fig. 20. Based on the S_{11} curve, we can calculate that the coupling factor of this coupler is 0.537 and the unloaded quality factor of the VHF gun is 31,700, which is close to the design value shown in Table III.

Second, the ports of Coupler 1 and Coupler 2 were connected to the two ports of the vector network analyzer, respectively. The S_{11} and S_{22} curves were repeatedly measured while the coupling loop of Coupler 2 was rotating, until the two curves completely overlapped, as shown in Fig. 21, indicating that these two couplers have the same coupling factor.

We found that the gun frequency decreases by about 100 kHz when the gun is pumped from the atmospheric state to the vacuum state. A simple calculation shows that the frequency should increase by 65 kHz due to media change from air to vacuum. Therefore, we can conclude that the deformation due to atmospheric pressure leads to a frequency reduction of about 165 kHz, which is slightly larger than the simulation prediction (100 kHz).

Furthermore, the resonant frequency tuning capability of the tuners was tested, as shown in Fig. 22. The forces of the four tuners were kept consistent during the tuning process. The resonant frequency was measured repeatedly when the forces of the tuners changed. The sum of the forces of the four tuners to the anode plate changed from approximately −44 up to 44 kN, during which the gun frequency increased. A linear fitting shows that the response of the gun frequency to the applied force is 2.149 kHz/kN in this process. Based on the measurements, the maximum tuning range of the tuners is approximately ±96 kHz.

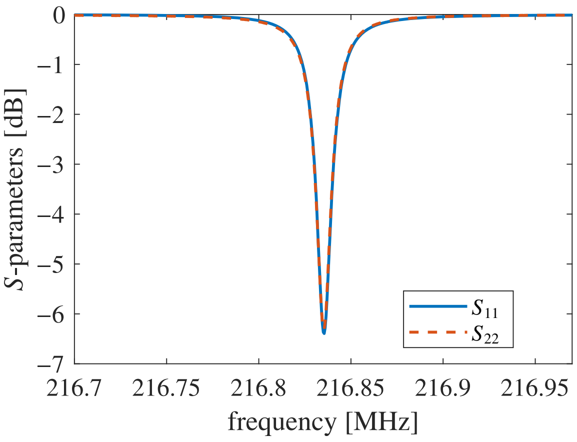

FIG. 21. S_{11} and S_{22} measurements with two coupler ports connected to two ports of the vector network analyzer, respectively.

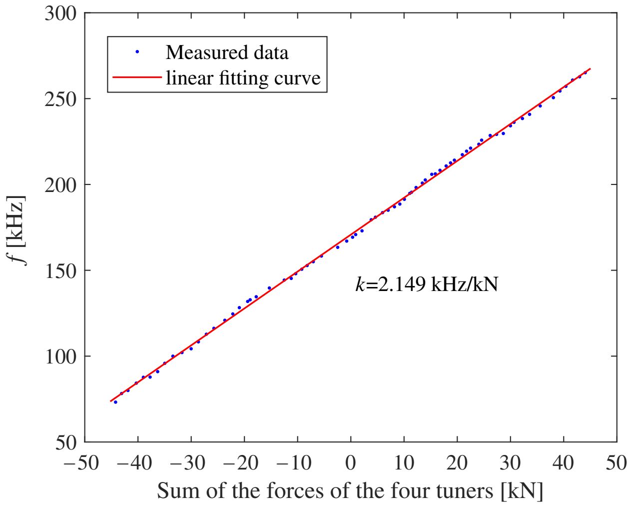

FIG. 22. The response of the gun resonant frequency with the force applied to the anode plate was measured to be 2.149 kHz/kN. f is the difference between the resonant frequency and the target frequency of 216.667 MHz. Negative values of the force represent pressure.

VII. HIGH POWER CONDITIONING

Each of the two coupler ports was connected to a 60 kW solid-state amplifier (SSA) via a 4–1/2 inch coaxial waveguide. The microwave generated by the SSA was transmitted through a waveguide and a coupler before being fed into the VHF gun. An LLRF system generated two rf signals, and each signal was used to drive an SSA. The amplitude and phase of the two driving signals were independently adjustable. During operation, the amplitude and phase of the two signals were adjusted so that the amplitude and phase of the two channels of rf power fed into the gun were the same, and thus the probe detected the maximum power in the gun.

Before high power conditioning, the gun was baked to achieve good vacuum performance. The stainless steel chamber of the gun was heated to 120 °C by wrapping conventional heating tapes. The large ion pump used a built-in heater to bake. The copper part of the gun was baked using rf heating [27]. During the rf baking, the water cooling of the gun was turned off completely, and the water cooling of the couplers remained open. The rf peak power fed into the gun was 30 kW, and the duty cycle was 10%, i.e., about 3 kW of average rf power was applied to the cavity. There were eight temperature probes on the cathode and anode plates to monitor the rise of the cavity temperature in real-time. The temperature of the cathode and anode plates was maintained at about 140 °C. Despite the absence of a temperature probe on the cathode nose, the temperature of the nose was anticipated to exceed 140 °C based on the simulated power density distribution on the cavity inner surface. After approximately 30 h of baking, all NEG pumps were activated and all ion pumps were turned on. At this time, the vacuum pressure in the gun without rf power was reduced to 2×10^{-8} Pa.

When the gun started to operate, the LLRF system worked in a self-excited loop mode, in which the frequency of the LLRF drive signals followed the resonant frequency of the gun. At the beginning, the VHF gun operated in pulse mode, with a pulse repetition rate of about 100 Hz. The peak power of the rf pulse was gradually increased. When the peak power reached a certain set power, the pulse width was increased until cw operation was achieved. It took approximately 130 integrated hours for the gun to reach 75 kW cw operation after initiating pulsed power conditioning.

In the pulsed operation mode, multipacting was observed in the gun under some gun powers. The multipacting intensity could be judged based on the distortion of the probe signals. The multipacting intensity varied with different rf powers. When the input power was below 23 kW, corresponding to a cathode gradient of 15 MV/m, the probe signal was distorted, indicating that multipacting had occurred. A typical probe signal when the input power was 4 kW and multipacting occurred is shown in Fig. 23(a). When the input power was larger than 23 kW, the probe signal was clean and stable, indicating that no multipacting had occurred. A typical probe signal without multipacting is shown in Fig. 23(b). The experimental results are consistent with the simulations shown in Fig. 4.

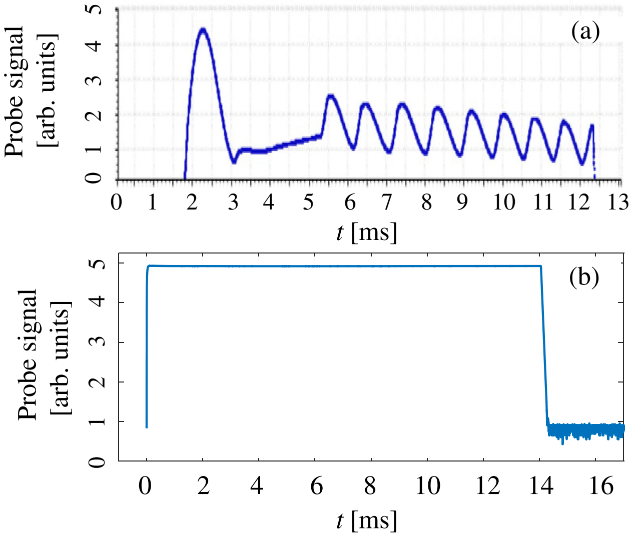

FIG. 23. Typical rf probe signals with (a) 4 kW input power corresponding to a 6.3 MV/m cathode gradient and (b) 27 kW input power corresponding to a 16.5 MV/m cathode gradient.

In addition, some current signals were detected by the microcurrent monitors on the couplers, as shown in Fig. 24. These current signals indicate the occurrence of multipacting in the couplers. The signal amplitude varied with different rf powers. Moreover, the signal amplitude was related to the vacuum pressure inside the coupler. The signal amplitude was larger with higher vacuum pressure. During the conditioning, it was found that the signal amplitude of Coupler 1 was always larger than that of Coupler 2, which was probably because the titanium nitride coating of Coupler 1 was thinner than that of Coupler 2, or some unknown contaminants inside Coupler 1 increased the emission of secondary electrons. In general, the current

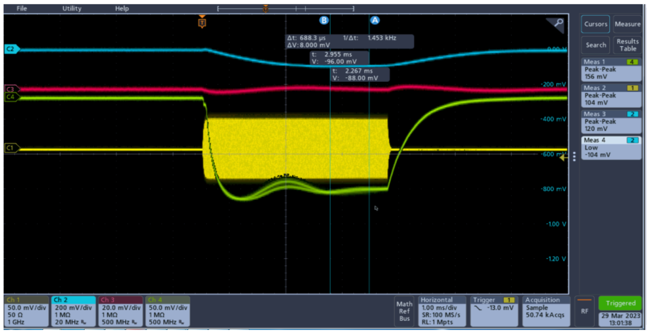

FIG. 24. Oscilloscope signals with rf power of 23 kW. The green and red lines are the current signals detected by the microcurrent monitors mounted on Coupler 1 and Coupler 2, respectively. The yellow line denotes the rf probe signal. The blue line is the dark current signal collected by a simple Faraday cup placed at the gun exit.

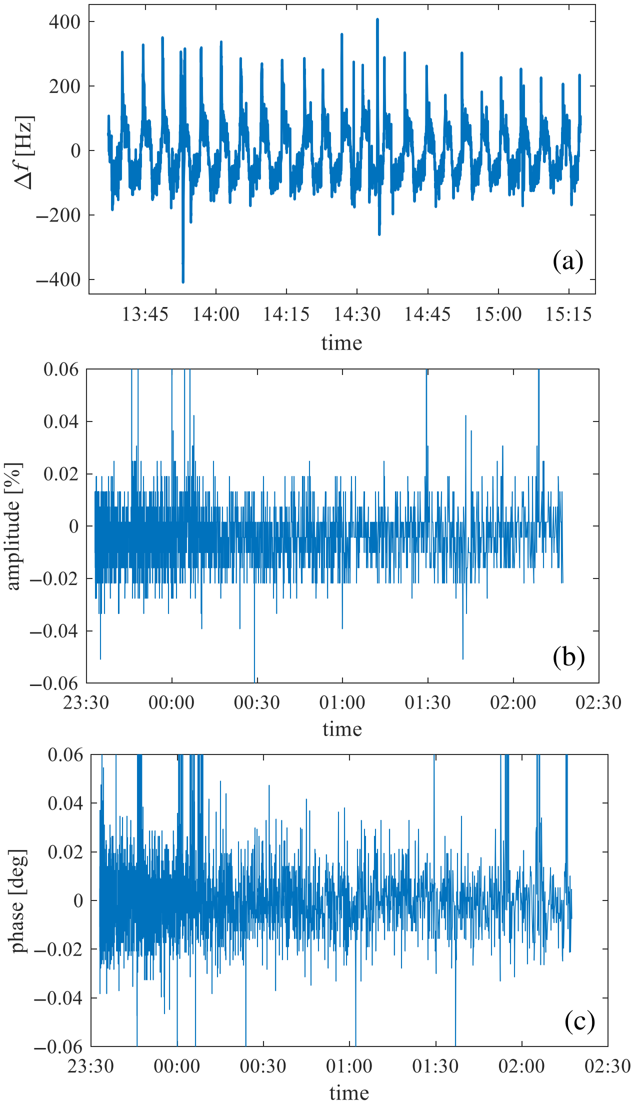

FIG. 25. (a) the change of the gun frequency within 1.5 h in active tuning mode. (b) the change of the amplitude of the probe signal within 3 h. (c) the change of the phase of the probe signal within 3 h. The input power is 75 kW.

signal with an amplitude of 1 μA or less was considered acceptable in pulse mode. Fortunately, the current signals of both couplers disappeared when operating in cw mode with 75 kW input power.

In the cw mode with 75 kW input power, the gun temperature gradually increased, and the resonant frequency gradually decreased. After about 4–5 h of warm-up, the gun frequency tended to stabilize. It was found that the gun frequency decreased by about 80 kHz during the warm-up period, which was a little larger than the simulation prediction (61 kHz for 90.4 kW input power). It was found that reducing the water flow rate of several cooling channels, especially the ones inside the nose, could increase thermal expansion and thus further reduce the frequency. In addition, baking the vacuum wall alone with heating tapes could also reduce the frequency, and the effect was even more significant than reducing the water flow. Preliminary experiments showed that heating the vacuum wall to 70 °C reduced the frequency by 150 kHz. These methods could be used when the gun frequency is out of the tuner tuning range. However, these methods are not recommended if the frequency is within the tuner tuning range, because the additional heat would deteriorate the vacuum and increase the operational instability. When the frequency was within the tuning range of the tuners, the tuners started to work to stabilize the gun frequency to 216.667 MHz. Figure 25(a) depicts the change of the gun frequency within 1.5 h in active tuning mode, and the gun frequency was stabilized between ±200 Hz. After frequency was locked, the LLRF system performed closed-loop control of the probe signal amplitude and phase. Figure 25(b) depicts the change of the amplitude of the probe signal within 3 h. The amplitude rms jitter with closed-loop control was 1.1 of ten thousand. Figure 25(c) depicts the change of the phase of the probe signal within 3 h. The phase rms jitter with closed-loop control was 0.0148°.

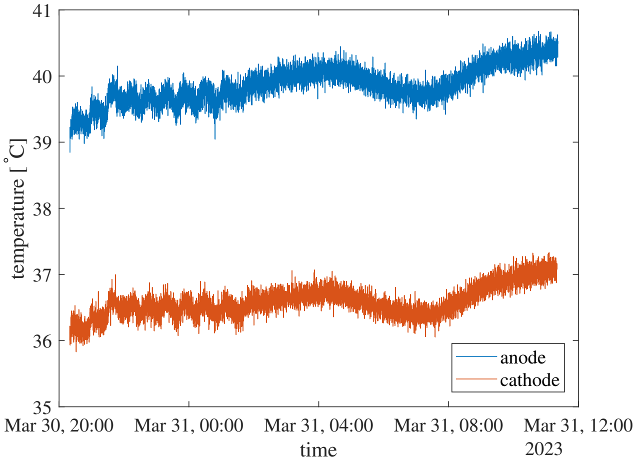

FIG. 26. The temperature change of the cathode and anode plates within 16 h of continuous high power conditioning. The input power is 75 kW.

Figure 26 shows the temperature change of the cathode and anode plates within 16 h of continuous high power conditioning. The temperature of the cathode plate was stabilized at about 37 °C, and the temperature of the anode plate was stabilized at about 40 °C. The vacuum pressure in the gun with the 75 kW input power was 9.8×10^{-8} Pa after one-day cw operation. The vacuum was expected to be better after longer-time operation.

Table IV summarizes what was achieved during the high power conditioning. cw stable operation was achieved with

TABLE IV. Rf performance during high power conditioning.

rf parameters	In design	Achieved
Operation mode	cw	cw
Cathode gradient (MV/m)	30	27
Input power (kW)	90.4	75
Voltage (keV)	868	780

an input power of 75 kW, corresponding to a cathode gradient of 27 MV/m. The gun voltage was 780 keV. The gun rf parameters have reached the SHINE requirements. However, further increases in rf power were constrained due to insufficient electrical system capacity at the gun test site. Although the design goal of 30 MV/m cathode gradient had not yet been reached, the operating gradient was already the highest in the world for room-temperature VHF guns.

VIII. BEAM COMMISSIONING

A diagnostic beamline was constructed for beam commissioning of the VHF gun, as depicted in Fig. 27. The VHF gun was situated at the beginning of the beamline. A cesium telluride photocathode was utilized during commissioning, which can be easily replaced using a load-lock system. A room-temperature 1.3 GHz 2-cell buncher was employed to compress the bunches. With careful water cooling design, the buncher could operate in cw mode. In offline tests, the buncher achieved cw operation at 14.4 kW input power, corresponding to a voltage of 340 kV. However, the 1.3 GHz solid-state power source of our test beamline could only deliver 6.5 kW rf power, limiting the buncher to operate at 230 kV voltage during beam commissioning. The resonant frequency of the buncher could be precisely adjusted by changing the water temperature of an independent water cooling unit.

The cathode was illuminated by a commercial laser to produce electron bunches. The laser wavelength is 257 nm. The initial full width at half maximum (FWHM) of the laser pulse was about 350 fs. The laser pulse was then broadened to about 11 ps FWHM by a transmission grating. Subsequently, the laser pulse was divided into two beams by a Glan prism, and the interval between pulses was adjusted by changing the length of the delay line. The beams were then combined to form a longitudinal stacked laser pulse with an FWHM of 22 ps. More Glan prisms can be employed to stack the pulses and create a longer laser pulse. However, due to the low compression voltage of the buncher, longer laser pulses pose challenges in compressing the electron beam to 1 mm rms. The repetition rate of the laser pulses was adjustable up to 1 MHz.

A solenoid (Solenoid 1 in Fig. 27) was placed at the exit of the gun for emittance compensation and beam focusing. In addition, another solenoid (Solenoid 2 in Fig. 27) was placed downstream of the buncher to provide additional focus for the electron beam. A Faraday cup was placed about 1.5 m downstream of the gun exit to measure the dark current and the photoelectron beam. Moreover, an integrated current transformer (ICT) was placed behind the Faraday cup to noninvasively measure the charge of the electron bunches. Downstream of Solenoid 2, a low-energy spectrometer, consisting of a dipole and a fluorescence imaging unit, was used to measure the energy of the electron beam at the exit of the gun and thus determine the gun voltage. Two 1.3 GHz room-temperature accelerating tubes (linacs) boosted the beam up to 28 MeV. At the end of the beamline, a high-energy spectrometer was used to measure the beam energy after the acceleration of the linacs. Downstream of the two linacs there were five quadrupoles and a deflecting cavity. The quadrupoles were used to focus the beam and perform the emittance measurements. The deflecting cavity was used to measure the bunch longitudinal distribution by applying a time-dependent vertical kick on the beam. Additionally, nine fluorescent screens mounted on motorized actuators in the beamline were used to measure the transverse distribution of the electron beam using CCD cameras.

It took several months for the installation of the VHF gun on the test beamline, the installation of the load-lock system, and the high power conditioning. After the conditioning was completed, the dark current was characterized. The dark current image on the first screen during the first round of electron beam experiments is shown in Fig. 28(a). It was found that the dark current primarily originates from two rings. The dark current in the inner ring emanates from the edge of the molybdenum plug, and the dark current in the outer ring originates from the edge of the copper iris. The dark current was then measured by the

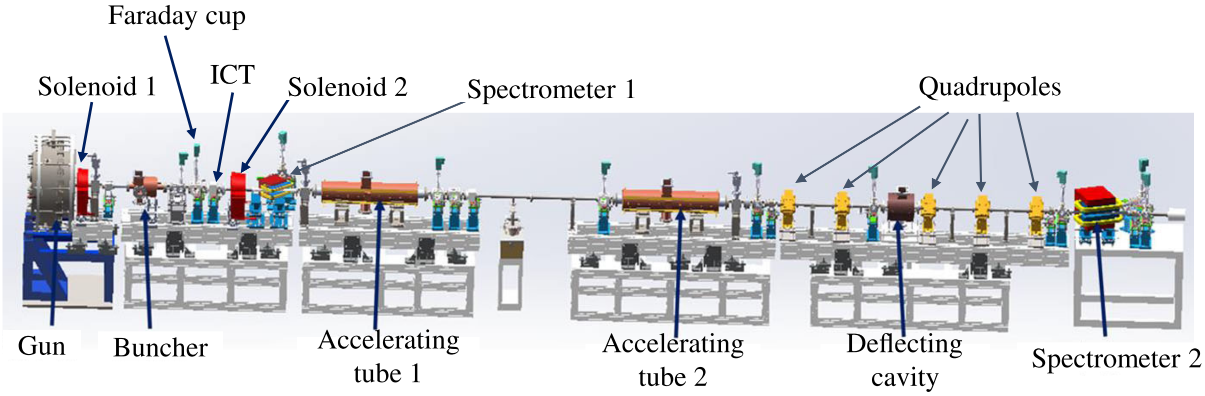

FIG. 27. Layout of the diagnostic beamline for the beam commissioning of the VHF gun.

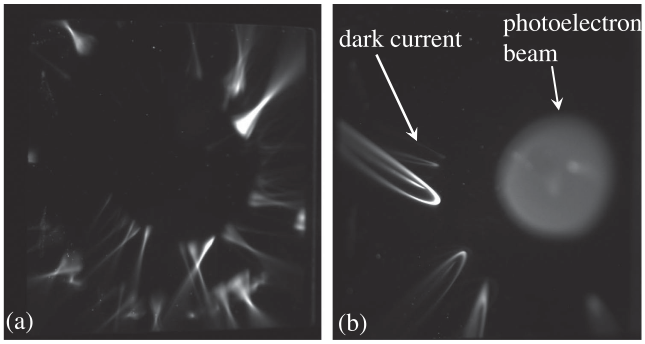

FIG. 28. (a) The dark current image on the first screen during the first round of experiments. The dark current in the inner ring comes from the edge of the molybdenum plug, while the dark current in the outer ring comes from the edge of the copper iris. (b) The dark current image on the first screen after ultrapure water rinsing. After the rinse, only a small amount of dark current from the copper iris remains. The photoelectron beam is also visible in the image.

Faraday cup. During the measurement, the strength of Solenoid 1 was scanned to maximize the collection of the dark current on the Faraday cup. The dark current was 14 μA for a cathode gradient of 27 MV/m. To identify the source of the dark current, we removed the used plug and observed it when replacing the cathode. Numerous scratches on the edge of the plug were discovered, which were caused by the plug rubbing against the stainless steel and copper pipes during the initial installation and collimation of the load-lock system. It was confirmed that these scratches were the source of the dark current in the inner ring, because when a new cathode was replaced, the dark current in the inner ring disappeared and the dark current collected by the Faraday cup was reduced to 6 μA. To figure out the source of the dark current in the outer ring, we removed the electron gun from the test beamline and performed ultrapure water rinse on all copper and stainless steel inner surfaces. When the electron gun was remounted on the beamline to measure the dark current, it was found that the dark current had become extremely low and the signal could not even be observed on the Faraday cup. After a few days of operation, the dark current image on the first screen was reexamined, as shown in Fig. 28(b). The dark current was still not observed on the molybdenum plug, while a small amount of dark current appeared on the copper iris. By scanning the strength of Solenoid 1, the maximum dark current was 376 nA. The aforementioned experiments demonstrate that ultrapure water rinsing can significantly reduce the dark current emission from the copper surface. We can conclude that the dark current emission at the copper iris is not caused by scratches or large surface roughness, as these issues cannot be resolved by water rinsing. From the dark current growth during gun operation, it is speculated that the dark current emission may be caused by the slow adhesion of dust from the test beamline to the gun copper iris, or by the ion back bombardment of the semiconductor cathode causing tellurium or cesium to adhere to the copper iris. The origin of the dark current at the copper iris still needs to be carefully studied.

The quantum efficiency of the cesium telluride cathode typically exceeded 10% when prepared in a deposition chamber. However, the cathode needed to be transported over long distances from the cathode preparation site to the test tunnel using a suitcase. The vacuum quality of the current suitcase was suboptimal, causing significant decay in the cathode's quantum efficiency during transport. Consequently, the cathode's quantum efficiency was typically around 1% upon insertion into the gun and commencement of electron beam production. The quantum efficiency of the cathode could be maintained above 0.5% for up to a month, which is acceptable in the current stage of beam commissioning. The energy of the laser pulse illuminating the cathode with full laser beam spot was about 200 nJ. Therefore, the gun could generate an electron beam with bunch charge of more than 200 pC. To improve the laser transverse uniformity, an aperture with a remotely exchangeable diameter was imaged onto the cathode plane through an image transfer system while optimizing beam brightness. Some of the laser pulse energy was blocked by the aperture. During the emittance measurement and optimization, the bunch charge was limited to 100 pC or less. Figure 29 presents a typical laser injection phase scan curve, which plots the bunch charge and beam energy at the gun exit as a function of the gun extraction phase.

The beam emittance was measured using a quadrupole scan method [38]. To measure the projected emittance, the intensity of the last quadrupole in the beamline was scanned while the change in the transverse beam size was measured on a yttrium aluminum garnet (YAG) screen 1.7 m downstream of the quadrupole. The thickness of the

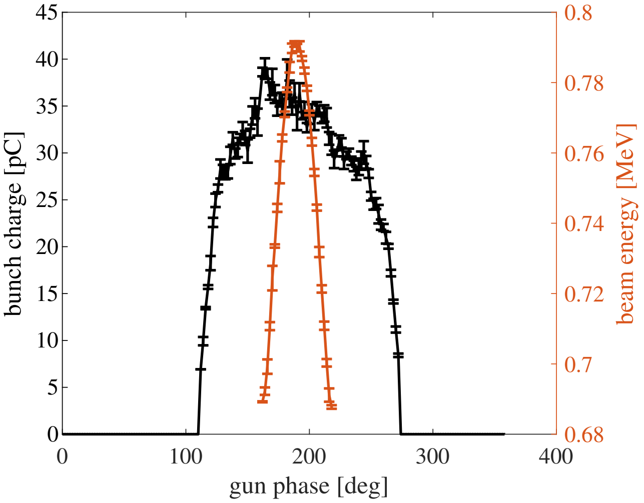

FIG. 29. Bunch charge and beam energy at the gun exit as a function of the laser injection phase. The buncher is turned off during the measurements.

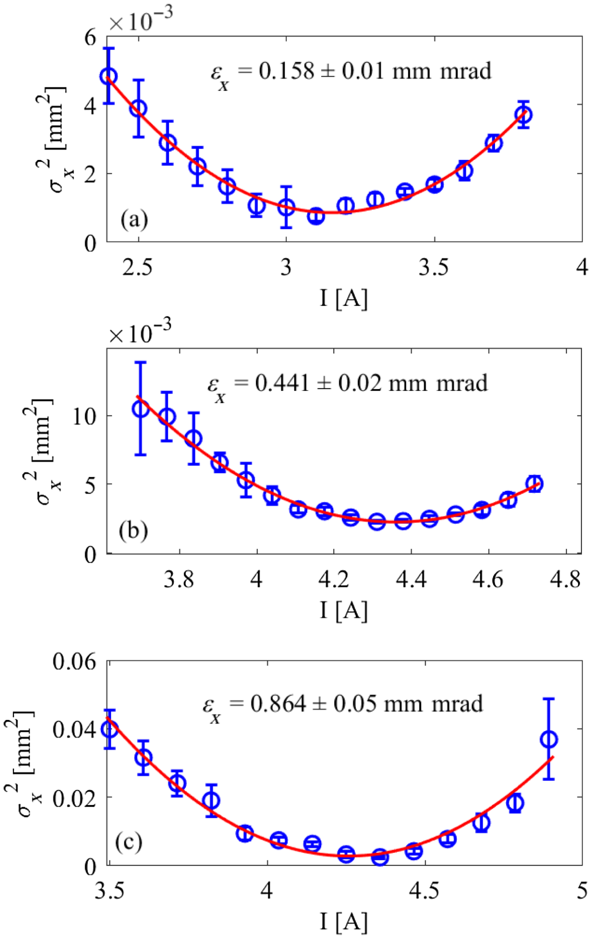

FIG. 30. Typical quadrupole scan curves for the projected emittance measurements of 10 pC (a), 50 pC (b), and 100 pC (c) electron bunches, respectively.

TABLE V. Emittance measurement results for different bunch charges.

Bunch charge (pC)	95% projected emittance (mm mrad)	95% sliced emittance (mm mrad)	Bunch length (mm rms)
10	0.161	0.154	0.49
50	0.429	0.383	1.15
100	0.853	0.842	1.44

YAG screen is 15 μm. To measure the sliced emittance, the deflecting cavity was turned on and kicked the beam in the vertical direction. The beam spot on the YAG screen was divided into 11 equal segments vertically, with the central one selected for calculating the transverse beam size. By fitting the transverse beam size and the quadrupole intensity, the beam moments and emittance can be calculated. During the measurement, the laser beam spot diameter was about 550 um. The VHF gun operated in a 10 Hz pulse mode with a cathode gradient of 27 MV/m. The beam energy at the location where the emittance measurements were performed was 28 MeV. An ASTRA [39] simulation shows that, due to space charge forces during quadrupole focusing and drifting, the projected emittance for a bunch charge of 100 pC will be overestimated by 20%, which is considered acceptable in the first stage of emittance measurements. Preliminary emittance optimization has been performed, including solenoid strength scan, laser injection phase scan, etc. Figure 30 depicts typical quadrupole scan curves for the projected emittance measurements of 10, 50, and 100 pC electron bunches. The projected and sliced emittances after optimization are summarized in Table V. The buncher was turned on during the measurements, and the compressed bunch length is also shown in Table V.

In our previous work on beam dynamics optimization based on ASTRA simulation [40,41], the optimum 95% projected normalized emittance for 100 pC bunches with a bunch length of 1 mm rms was below 0.1 mm mrad. However, the measured emittance was noticeably larger than the simulated value. This discrepancy can be attributed to several factors. The laser longitudinal length in the experiment is shorter than that in the simulation. The laser transverse distribution is not as uniform as in the simulation. The spherical aberration of the currently used solenoid is larger than that in the simulation. The buncher voltage is lower than the simulated value, and the buncher phase needs to be lower to compress bunches to the target length, which is also not conducive to emittance preservation. In addition, the difference between the slice emittance and the projected emittance in the measurements is not large, which is probably caused by the fact that the voltage of the deflecting cavity is not high enough, making too little separation between the bunch head and tail. More comprehensive emittance optimization will be performed in the next phase of beam commissioning, with the potential to obtain lower emittance.

When the gun operated in cw mode, electron bunches with a maximum repetition rate of 10 kHz and a charge of up to 100 pC were steadily produced. However, we did not continue to increase the repetition rate in the first phase of the commissioning concerned about possible damage to the laser and optical transmission elements. Increasing the repetition rate is expected in the second phase of the experiment.

IX. SUMMARY AND OUTLOOK

SHINE is an MHz-class high-repetition-rate XFEL facility in China, which requires an electron source operating in cw mode. Based on the experience with the APEX gun, the VHF gun has emerged as a relatively mature solution for the SHINE electron source. Tsinghua University has been developing the VHF gun for SHINE since the end of 2018. After four years of effort, the gun was successfully developed and installed in the SHINE tunnel. This paper provides a detailed description of the gun's physical design, including the optimization of the input power, surface electric field, surface power density, the suppression of multipacting, and the analysis of thermal effects. In addition, the mechanical design, including the VHF gun itself, the frequency tuners, the rf power couplers, the rf probes, is also introduced. The quality factor measured in the cold test was 31700, which is 94% of the design value. During high power conditioning, the tuners can adjust the gun frequency to the target frequency of 216.667 MHz. The multipacting intensity occurring in the gun, varying with the cathode gradient, closely resembles the simulations. A cw rf power of 75 kW has been successfully fed into the gun. The cathode gradient reached about 27 MV/m and the gun voltage reached about 780 keV. With the support of the LLRF system working in closed-loop control mode, the amplitude rms jitter is 1.1 out of 10,000, and the phase rms jitter is 0.0148°. A test beamline was constructed to measure and optimize the beam quality. We found that ultrapure water rinsing significantly reduced dark current emission from the copper surface. After rinsing, the maximum dark current collected by the Faraday cup at the gun exit is less than 376 nA when scanning the strength of the gun solenoid. After preliminary optimization, the 95% projected transverse emittance was 0.161 mm mrad for 10 pC bunches with bunch length of 0.49 mm rms, 0.429 mm mrad for 50 pC bunches with bunch length of 1.15 mm rms, and 0.853 mm mrad for 100 pC bunches with bunch length of 1.44 mm rms. At the same bunch length, the 95% sliced transverse emittance was 0.154 mm mrad for 10 pC bunches, 0.383 mm mrad for 50 pC bunches, and 0.842 mm mrad for 100 pC bunches.

A new version of the coupler is being manufactured and will be mounted on the gun soon. The new coupler has a new choke structure near the ceramic window, which is expected to further enhance the safety of the coupler operation. In addition, permanent solenoid magnets have been designed and will be installed on the coupler waveguides in the next phase of experiments to suppress the multipacting in the couplers. In the next phase of experiments, the beam brightness will continue to be optimized, and the ability to generate a 1 MHz repetition rate beam will be tested.

ACKNOWLEDGMENTS

This work is supported by the National Natural Science Foundation of China (NSFC) under Grant No. 12275149. It is also funded by the Tsinghua University Initiative Scientific Research Program No. 20197050028, No. 20191081195.

---

[1] E. Prat, R. Abela, M. Aiba, A. Alarcon, J. Alex, Y. Arbelo, C. Arrell, V. Arsov, C. Bacellar, C. Beard *et al.*, A compact and cost-effective hard x-ray free-electron laser driven by a high-brightness and low-energy electron beam, Nat. Photonics **14**, 748 (2020).

[2] J. Amann, W. Berg, V. Blank, F.-J. Decker, Y. Ding, P. Emma, Y. Feng, J. Frisch, D. Fritz, J. Hastings *et al.*, Demonstration of self-seeding in a hard-x-ray free-electron laser, Nat. Photonics **6**, 693 (2012).

[3] Z. Zhao, D. Wang, L. Yin, Q. Gu, G. Fang, M. Gu, Y. Leng, Q. Zhou, B. Liu, C. Tang *et al.*, Shanghai soft x-ray free-electron laser facility, Chin. J. Lasers **46**, 0100004 (2019).

[4] W. Decking, S. Abeghyan, P. Abramian, A. Abramsky, A. Aguirre, C. Albrecht, P. Alou, M. Altarelli, P. Altmann, K. Amyan *et al.*, A mhz-repetition-rate hard x-ray free-electron laser driven by a superconducting linear accelerator, Nat. Photonics **14**, 391 (2020).

[5] A. Picón, C. Lehmann, C. Bostedt, A. Rudenko, A. Marinelli, T. Osipov, D. Rolles, N. Berrah, C. Bomme, M. Bucher *et al.*, Hetero-site-specific x-ray pump-probe spectroscopy for femtosecond intramolecular dynamics, Nat. Commun. **7**, 11652 (2016).

[6] C. Gisriel, J. Coe, R. Letrun *et al.*, Membrane protein megahertz crystallography at the European XFEL, Nat. Commun. **10**, 5021 (2019).

[7] H. N. Chapman, P. Fromme, A. Barty, T. A. White, R. A. Kirian, A. Aquila, M. S. Hunter, J. Schulz, D. P. DePonte, U. Weierstall *et al.*, Femtosecond x-ray protein nanocrystallography, Nature (London) **470**, 73 (2011).

[8] D. Milathianaki, S. Boutet, G. Williams, A. Higginbotham, D. Ratner, A. Gleason, M. Messerschmidt, M. M. Seibert, D. Swift, P. Hering *et al.*, Femtosecond visualization of lattice dynamics in shock-compressed matter, Science **342**, 220 (2013).

[9] J. Stohr, Linac coherent light source II (LCLS-II) conceptual design report, SLAC National Accelerator Lab., Menlo Park, CA, USA, Technical Report No. SLAC-R-978, 2011).

[10] N. Huang, H. Deng, B. Liu, D. Wang *et al.*, Physical design and fel performance study for FEL-III beamline of SHINE, in *Proceedings of the 39th International Free Electron Laser Conference, Hamburg, Germany* (JACoW, Geneva, Switzerland, 2019), pp. 26–30.

[11] V. Paramonov, S. Philipp, I. Rybakov, A. Skassyrskaya, and F. Stephan, Design of an L-band normally conducting RF gun cavity for high peak and average RF power, Nucl. Instrum. Methods Phys. Res., Sect. A **854**, 113 (2017).

[12] G. Shu, H. Qian, N. Aftab, P. Boonpornprasert, G. Georgiev, J. Good, M. Gross, C. Koschitzki, M. Krasilnikov, A. Lueangaramwong *et al.*, Dark current studies of an L-band normal conducting RF gun, Nucl. Instrum. Methods Phys. Res., Sect. A **1010**, 165546 (2021).

[13] C. Gulliford, A. Bartnik, I. Bazarov, B. Dunham, and L. Cultrera, Demonstration of cathode emittance dominated high bunch charge beams in a DC gun-based photoinjector, Appl. Phys. Lett. **106**, 094101 (2015).

[14] C. Hernandez-Garcia, T. Siggins, S. Benson, D. Bullard, H. Dylla, K. Jordan, C. Murray, G. Neil, M. Shinn, and R. Walker, A high average current DC GaAs photocathode gun for ERLs and FELs, in *Proceedings of the 2005 Particle Accelerator Conference* (IEEE, New York, 2005), pp. 3117–3119.

[15] R. Wells, W. Ghiorso, J. Staples, T. Huang, F. Sannibale, and T. Kramasz, Mechanical design and fabrication of the

VHF-gun, the Berkeley normal-conducting continuous-wave high-brightness electron source, Rev. Sci. Instrum. **87**, 023302 (2016).

[16] L. Zheng, Z. Li, Y. Du, H. Chen, B. Gao, R. Li, W. Huang, and C. Tang, Design of a 217 MHz VHF gun at Tsinghua University, in *Proceedings of the 10th International Particle Accelerator Conference (IPAC'19), Melbourne, Australia, 2019* (JACoW Publishing, Geneva, Switzerland, 2019), pp. 2050–2053.

[17] G. Shu, Y. Chen, S. Lal, H. Qian, H. Shaker, F. Stephan *et al.*, First design studies of a NC CW RF gun for European XFEL, in *Proceedings of the 10th International Particle Accelerator Conference (IPAC'19)* (JACoW, Geneva, 2019), pp. 1698–1701.

[18] C. Wang, Z.-H. Zhu, Z.-G. Jiang, Q.-S. Tang, Z.-T. Zhao, and Q. Gu, Design of a 162.5 MHz continuous-wave normal-conducting radiofrequency electron gun, Nucl. Sci. Tech. **31**, 1 (2020).

[19] I. Petrushina, V. Litvinenko, Y. Jing, J. Ma, I. Pinayev, K. Shih, G. Wang, Y. Wu, Z. Altinbas, J. Brutus *et al.*, High-brightness continuous-wave electron beams from superconducting radio-frequency photoemission gun, Phys. Rev. Lett. **124**, 244801 (2020).

[20] A. Arnold and J. Teichert, Overview on superconducting photoinjectors, Phys. Rev. ST Accel. Beams **14**, 024801 (2011).

[21] E. Wang, V. N. Litvinenko, I. Pinayev *et al.*, Long lifetime of bialkali photocathodes operating in high gradient superconducting radio frequency gun, Sci. Rep. **11**, 4477 (2021).

[22] D. Janssen, H. Büttig, P. Evtushenko, M. Freitag, F. Gabriel, B. Hartmann, U. Lehnert, P. Michel, K. Möller, T. Quast *et al.*, First operation of a superconducting RF-gun, Nucl. Instrum. Methods Phys. Res., Sect. A **507**, 314 (2003).

[23] C. Hernandez-Garcia, D. Bullard, F. Hannon, Y. Wang, and M. Poelker, High voltage performance of a dc photoemission electron gun with centrifugal barrel-polished electrodes, Rev. Sci. Instrum. **88**, 093303 (2017).

[24] R. Nagai, R. Hajima, N. Nishimori, T. Muto, M. Yamamoto, Y. Honda, T. Miyajima, H. Iijima, M. Kuriki, M. Kuwahara *et al.*, High-voltage testing of a 500-kv dc photocathode electron gun, Rev. Sci. Instrum. **81**, 033304 (2010).

[25] G. Gevorkyan, C. Sarabia-Cardenas, A. Kachwala, C. Knill, T. J. Hanks, P. Bhattacharyya, W. H. Li, L. Cultrera, A. Galdi, I. Bazarov *et al.*, A cryogenically cooled 200 kv DC photoemission electron gun for ultralow emittance photocathodes, Rev. Sci. Instrum. **94**, 091501 (2023).

[26] R. Xiang, Y. Ding, K. Zhao, X. Lu, S. Quan, B. Zhang, L. Wang, S. Huang, L. Lin, and J. Chen, Experimental investigations of DC-SC photoinjector at Peking University, Nucl. Instrum. Methods Phys. Res., Sect. A **528**, 321 (2004).

[27] F. Sannibale, D. Filippetto, C. Papadopoulos, J. Staples, R. Wells, B. Bailey, K. Baptiste, J. Corlett, C. Cork, S. De Santis *et al.*, Advanced photoinjector experiment photogun commissioning results, Phys. Rev. ST Accel. Beams **15**, 103501 (2012).

[28] F. Sannibale, D. Filippetto, H. Qian, C. Mitchell, F. Zhou, T. Vecchione, R. Li, S. Gierman, and J. Schmerge, High-brightness beam tests of the very high frequency gun at the advanced photo-injector experiment test facility at the Lawrence Berkeley National Laboratory, Rev. Sci. Instrum. **90**, 033304 (2019).

[29] F. Zhou, C. Adolphsen, A. Benwell, G. Brown, D. Dowell, M. Dunning, S. Gilevich, K. Grouev, G. Huang, B. Jacobson *et al.*, Commissioning of the SLAC linac coherent light source II electron source, Phys. Rev. Accel. Beams **24**, 073401 (2021).

[30] S.-H. Kim, Protection of accelerator hardware: RF systems, arXiv:1608.03096.

[31] J.-H. Han, K. Flöttmann, and W. Hartung, Single-side electron multipacting at the photocathode in rf guns, Phys. Rev. ST Accel. Beams **11**, 013501 (2008).

[32] J.-H. Han, M. Krasilnikov, and K. Flöttmann, Secondary electron emission in a photocathode rf gun, Phys. Rev. ST Accel. Beams **8**, 033501 (2005).

[33] B. Henrist, C. Scheuerlein, N. Hilleret, M. Taborelli, and G. Vorlaufer, The variation of the secondary electron yield and of the desorption yield of copper under electron bombardment: Origin and impact on the conditioning of the LHC, Technical Report No. LHC-Project-Report-583, 2002.

[34] V. Baglin, J. Bojko, O. Gröbner, B. Henrist, N. Hilleret, C. Scheuerlein, and M. Taborelli, The secondary electron yield of technical materials and its variation with surface treatments, Technical Report No. LHC-Project-Report-433, 2000.

[35] R. Huang, D. Filippetto, C. Papadopoulos, H. Qian, F. Sannibale, and M. Zolotorev, Dark current studies on a normal-conducting high-brightness very-high-frequency electron gun operating in continuous wave mode, Phys. Rev. ST Accel. Beams **18**, 013401 (2015).

[36] M. Ady and R. Kersevan, Introduction to the latest version of the test-particle Monte Carlo code molflow+, in *Proceedings of the 5th International Particle Accelerator Conference (IPAC'14)* (JACoW, Geneva, 2014), p. 2348.

[37] ANSYS, https://www.ansys.com/.

[38] L. Zheng, Y. Du, Z. Zhang, H. Qian, L. Yan, J. Shi, Z. Zhang, Z. Zhou, X. Wu, X. Su, D. Wang, Q. Tian, W. Huang *et al.*, Development of S-band photocathode RF guns at Tsinghua University, Nucl. Instrum. Methods Phys. Res., Sect. A **834**, 98 (2016).

[39] K. Floettmann, ASTRA—A space charge tracking algorithm, https://www.desy.de/mpyflo/.

[40] H. Chen, L.-M. Zheng, B. Gao, Z.-Z. Li, Y.-C. Du, R.-K. Li, W.-H. Huang, C.-X. Tang, D. Gu, Z. Qi, M. Zhang, H.-X. Deng, Q. Gu, and D. Wang, Beam dynamics optimization of very-high-frequency gun photoinjector, Nucl. Sci. Tech. **33**, 116 (2022).

[41] H. Chen, L. Zheng, P. Huang, C. Song, Y. Du, R. Li, W. Huang, and C. Tang, Analysis of slice transverse emittance evolution in a very-high-frequency gun photoinjector, Phys. Rev. Accel. Beams **24**, 124402 (2021).